

# RSC Advances



This is an *Accepted Manuscript*, which has been through the Royal Society of Chemistry peer review process and has been accepted for publication.

*Accepted Manuscripts* are published online shortly after acceptance, before technical editing, formatting and proof reading. Using this free service, authors can make their results available to the community, in citable form, before we publish the edited article. This *Accepted Manuscript* will be replaced by the edited, formatted and paginated article as soon as this is available.

You can find more information about *Accepted Manuscripts* in the [Information for Authors](#).

Please note that technical editing may introduce minor changes to the text and/or graphics, which may alter content. The journal's standard [Terms & Conditions](#) and the [Ethical guidelines](#) still apply. In no event shall the Royal Society of Chemistry be held responsible for any errors or omissions in this *Accepted Manuscript* or any consequences arising from the use of any information it contains.

Cite this: DOI: 10.1039/c0xx00000x

www.rsc.org/xxxxxx

ARTICLE TYPE

## Ternary Alloy Nanocrystals of Tin and Germanium Chalcogenides

Hyung Soon Im, Yoon Myung, Kidong Park, Chan Su Jung, Young Rok Lim, Dong Myung Jang, and Jeunghye Park\*

Received (in XXX, XXX) Xth XXXXXXXXX 20XX, Accepted Xth XXXXXXXXX 20XX

DOI: 10.1039/b000000x

Tin (Sn) and germanium (Ge) chalcogenides have recently gained popularity as potential alternatives to the toxic lead chalcogenides, due in part to their relatively higher chemical and environmental stability, for use in photovoltaic devices. Herein, we report the synthesis of ternary composition chalcogenide, *i.e.*,  $\text{Sn}_x\text{Ge}_{1-x}\text{S}$ ,  $\text{Sn}_x\text{Ge}_{1-x}\text{Se}$ ,  $\text{GeS}_x\text{Se}_{1-x}$ , and  $\text{SnS}_x\text{Se}_{1-x}$ , nanocrystals (NCs) by novel gas-phase laser photolysis. A full series of completely miscible alloy nanocrystals, the band gaps of which could be tuned to cover a wide range (0.9–1.6 eV), were obtained by facile composition tuning through adept control of the relative pressure of the precursors. Two cation alloy ( $\text{Sn}_x\text{Ge}_{1-x}\text{S}$  and  $\text{Sn}_x\text{Ge}_{1-x}\text{Se}$ ) NCs exhibited unique anisotropic bowing phenomena of the orthorhombic phase lattice constants, but the anion alloy ( $\text{GeS}_x\text{Se}_{1-x}$  and  $\text{SnS}_x\text{Se}_{1-x}$ ) NCs did not. The cation alloy NCs showed the optical bowing, which is well correlated with the bowing of the lattice parameters. The  $\text{Sn}_x\text{Ge}_{1-x}\text{S}$  and  $\text{SnS}_x\text{Se}_{1-x}$  NCs showed remarkably higher photoconversion efficiency in photovoltaic and photodetector devices when compared with that of end members.

### 15 Introduction

IV–VI chalcogenide semiconductor nanocrystals (NCs) have attracted considerable attention in photovoltaic applications owing to their unique size-dependent optical and electrical properties.<sup>1–4</sup> Recently, there has been increased interest in the ternary alloys of IV–VI chalcogenide semiconductors, as they offer the exceptional advantage of modifying the properties of semiconductors for specific applications. In particular, alloying is considered to be an effective strategy in solar energy conversion devices for controlling the conduction band gap offsets and/or localized defect energy levels, which is critical for achieving high photoconversion efficiency. However, it is highly challenging to realize homogeneous alloys because of the inherent differences in precursor reaction kinetics, which require adept control of the reactivity of individual precursors. Thus far, limited success has been reported in the following systems:  $\text{PbSSe}$ ,  $\text{PbSnTe}$ ,  $\text{PbSnS}$ ,  $\text{PbSTe}$ ,  $\text{PbSeTe}$ ,  $\text{SnSSe}$ ,  $\text{GeSSe}$ , and  $\text{SnGeSe}$ .<sup>5–19</sup>

Lately, tin and germanium chalcogenides ( $\text{SnS}$ ,  $\text{SnSe}$ ,  $\text{GeS}$ , and  $\text{GeSe}$ ) have gained popularity as potential alternatives to the conventional lead chalcogenides in part because of their relatively higher chemical and environmental stability as compared to more toxic lead chalcogenides. Typically, tin and germanium chalcogenides possess a thermodynamically preferred orthorhombic crystal structure, described as a highly distorted rock salt structure consisting of strongly bound double layers held by a weaker van der Waals force. They are native *p*-type semiconductors with high absorption coefficient, and narrow band gap; the band gap of bulk materials being  $E_g = 1.5\text{--}1.6$  eV ( $\text{GeS}$ ),  $1.1\text{--}1.2$  eV ( $\text{GeSe}$ ),  $1.1$  eV ( $\text{SnS}$ ), and  $0.9$  eV ( $\text{SnSe}$ ).<sup>20–25</sup> The band gaps of  $\text{SnGeS}$ ,  $\text{SnGeSe}$ ,  $\text{SnSe}$ , and  $\text{GeSSe}$  alloys covered the wide range of  $0.9\text{--}1.6$  eV. Recently, Wei *et al.* synthesized  $\text{SnS}_x\text{Se}_{1-x}$  NCs using a solution reaction of  $\text{SnO}_2$ , S, and Se.<sup>16</sup> Brutchey and co-workers reported the synthesis of

composition-tuned  $\text{Sn}_x\text{Ge}_{1-x}\text{Se}$  NCs in solution phase.<sup>18</sup> Nevertheless, development of facile strategies for controlling the composition of both cation and anion alloys is still a critical requirement.

In the present work, we demonstrate the successful synthesis of ternary alloy series;  $\text{Sn}_x\text{Ge}_{1-x}\text{S}$ ,  $\text{Sn}_x\text{Ge}_{1-x}\text{Se}$ ,  $\text{GeS}_x\text{Se}_{1-x}$ , and  $\text{SnS}_x\text{Se}_{1-x}$  NCs, with controlled composition over the whole range of  $0 \leq x \leq 1$ . The ligand-free NCs were synthesized by the gas-phase laser photolysis method, wherein the composition of the NCs could be easily tuned by controlling the partial pressure of the reactant mixture. This method has previously been adopted for the synthesis of anion alloy NCs.<sup>17,19</sup> Herein, we extend this method to the composition tuning of cation alloys, which has not been attempted yet. Thus far, several researchers have analyzed the optoelectronic properties of  $\text{GeSe}$ ,  $\text{SnS}$ , and  $\text{SnSe}$  nanostructures, including nanosheets and nanowires, demonstrating their promising potential in photovoltaic applications.<sup>26–39</sup> We report here the enhanced photoconversion efficiency of the alloy NCs in photoelectrochemical (PEC) cells and photodetector devices when compared with that of the binary counterparts. In order to understand such an enhancement effect, we thoroughly examined the dependence of the lattice parameters and optical band gap on the composition. We believe that the results obtained in this study will pave the way for the development of frontier photovoltaic devices.

### Experimental Section

Laser photolysis of  $(\text{Ge}(\text{CH}_3)_4, \text{TMG})$ , tetramethyl tin ( $\text{Sn}(\text{CH}_3)_4, \text{TMT}$ ), hydrogen sulfide ( $\text{H}_2\text{S}$ ), and dimethyl selenium ( $\text{Se}(\text{CH}_3)_2, \text{DMS}$ ) was performed using an Nd:YAG pulsed laser (Coherent) operated at 1064 nm, with a repetition rate of 10 Hz and a pulse width of 10 ns. All the precursors were purchased from Sigma-Aldrich or Alfa Co. The precursors were degassed by

several freeze (77 K)-pump-thaw cycles, and used without further purification. In the typical process, the precursor vapors (<300 Torr) were introduced to a Pyrex glass reactor, equipped with a gas valve connected to a standard vacuum line and a quartz optical window. The laser beam was focused into the reactor through the quartz window, by using a lens of focal length 10 cm. The experiment was carried out using the photon energy of 0.1–0.2 J/pulse. After 1 h of laser irradiation, the gas products were vented out. Subsequently, the NCs were collected by dispersing them in ethanol, followed by evaporation and vacuum drying at room temperature. In order to obtain the crystalline phase, the obtained NC powders were thermally annealed in a quartz tube under vacuum at 350–450°C for 1 h.

Graphene oxide (GO) was synthesized from graphite by Hummer's exfoliation method, which was further reduced using H<sub>2</sub> gas at 800°C to obtain reduced GO (RGO). The NC-RGO hybrid nanostructures were subsequently prepared by mixing NCs with RGO in isopropyl alcohol (IPA) under sonication, and then precipitated and dried. The average thickness of the RGO sheets, as determined by using AFM (Park System XE100), was 6 nm.

The samples were characterized by scanning electron microscopy (SEM, Hitachi S-4700), field-emission transmission electron microscopy (TEM, Jeol JEM 2100F and FEI TECNAI G<sup>2</sup> 200 kV), high-voltage TEM (HVEM, Jeol JEM ARM 1300S, 1.25 MV), and energy-dispersive X-ray spectroscopy (EDX). High-resolution X-ray diffraction (XRD) patterns were obtained using the 9B and 3D beam lines of the Pohang Light Source (PLS) with monochromatic radiation ( $\lambda = 1.5474 \text{ \AA}$ ). UV-visible-NIR absorption spectra of the samples were recorded using a spectrometer (Cary 5000, Agilent Tech.). The Raman spectra were measured using the 514.5 nm line of an argon ion laser.

The cyclic voltammetry (CV) curves were recorded on an IVIUM CompactStat electrochemical analyzer using gold (area ca. 0.02 cm<sup>2</sup>) disks as the working electrode, Pt-wire as auxiliary electrode and Ag/0.01 M AgNO<sub>3</sub> as reference electrode (BAS Inc., 0.1 M tetrabutylammonium hexafluorophosphate (TBAPF<sub>6</sub>)/acetonitrile electrolyte). The NC solution was prepared by dispersing 1 mg of NC in 1 mL of IPA. Approximately a drop of the NC solution was placed on the polished surface of the working electrode, and the solvent was then evaporated to form a film. The electrolytes were thoroughly deoxygenated by bubbling with high-purity Ar gas for 15 min. The valence band (VB) and conduction band (CB) energies,  $E_{VB}$  and  $E_{CB}$ , respectively, can be calculated from the voltage values corresponding to the onset of oxidation peak ( $E_{Ox}$ ) and reduction ( $E_{Red}$ ) peak, assuming the energy level of ferrocene/ferrocenium (Fc/Fc<sup>+</sup>) to be -4.8 eV below the vacuum level. The formal potential of Fc/Fc<sup>+</sup> was measured to be 0.085 V against an Ag/Ag<sup>+</sup> reference electrode, providing the calibration equations,  $E_{VB} = -(E_{Ox} + 4.715) \text{ eV}$ ;  $E_{CB} = -(E_{Red} + 4.715) \text{ eV}$ .

Transient photocurrents of the photoelectrochemical (PEC) cells were measured in a three-electrode setup composed of 0.5 M sodium sulfate (Na<sub>2</sub>SO<sub>4</sub>) aqueous electrolyte, Pt foil counter electrode, and Ag/AgCl reference electrode (Aldrich, 3 M KCl). In the typical process, 100 mg of the NCs was dissolved in 5 mL of IPA. Typically, about 60 min of ultrasonication was necessary to obtain uniformly dispersed solution. The NC film was

fabricated by dropping 100  $\mu\text{L}$  of the NC solution onto an area of 0.25 cm<sup>2</sup> in the ITO substrate, followed by drying under ambient conditions. A constant light intensity of 100 mW/cm<sup>2</sup> from a 450 W Xe lamp (Oriel) passed through an AM 1.5G filter was used as the light source. The photo-response of the NC films was applied at -0.5 V vs. Ag/AgCl at 10 s on/off chopped illuminations.

The Ti (20 nm)/Au (80 nm) film electrode was deposited onto a Si substrate with a thermally grown SiO<sub>2</sub> layer of thickness 1  $\mu\text{m}$ , by sputtering using a patterned mask. The gap between the electrodes was 1.5  $\mu\text{m}$ . The photodetector was then fabricated by using the dielectrophoresis (DEP) technique. We tested the devices on the probe station with parametric test equipment (Agilent E5270A) at room temperature, using 514 nm Ar ion laser (2–20 mW) or light emitting diode (LED) operating at 850 nm (max. 170 mW) as the light source.

## Results and Discussion

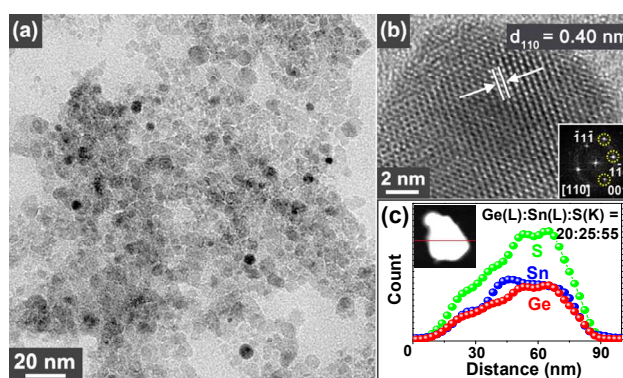


**Fig. 1** (a) HRTEM image revealing the spherical shape of Sn<sub>0.6</sub>Ge<sub>0.4</sub>S NCs. The average diameter is 10 nm. (b) Lattice-resolved and FFT images (at the zone axis of [110]) of selected orthorhombic phase NCs shows  $d_{110} = 4.0 \text{ \AA}$ . (c) EDX line-scan profile showing the homogeneous distribution of the elements Sn, Ge, and S along the cross section of NC (whose STEM is shown in the inset) in a ratio of 25:20:55.

Table S1 (ESI<sup>†</sup>) summarizes the partial pressure of the precursors for all the NCs (total 56 samples) prepared in the present work. The overall morphology was observed by using TEM (Fig. 1a). The NCs exhibit a size distribution with an average diameter of  $10 \pm 3 \text{ nm}$ . Fig. 1b shows the lattice-resolved and corresponding fast-Fourier transform (FFT) images (zone axis = [110]) of orthorhombic phase Sn<sub>0.6</sub>Ge<sub>0.4</sub>S. The  $d$ -spacing of the (110) planes is estimated to be 4.0  $\text{\AA}$ , which is consistent with the value calculated by Vegard's rule using the bulk values  $d_{\text{SnS}(110)} = 4.04 \text{ \AA}$  and  $d_{\text{GeS}(110)} = 3.97 \text{ \AA}$ . The EDX line scan profile of Sn (L shell), Ge (L shell), and S (K shell) showed an elemental ratio of 25:20:55, along the cross section of the NC. Inset corresponds to the scanning TEM (STEM) image of the NCs.

Fig. S1 (ESI<sup>†</sup>) shows the XRD patterns of the NCs. The peaks were assigned to those of orthorhombic phase with a *Pnma* or *Pbnm* space group. The composition ( $x$ ) of alloy NCs was determined using Vegard's law (*i.e.*,  $d = (1 - x)d_{\text{GeS}} + xd_{\text{SnS}}$ ) based on the peak position of the end members. For this, approximately 5–8 high-intensity peaks were selected to calculate the composition, and their average value was determined as  $x$ . The  $x$  value was found to be consistent with the corresponding EDX data shown in the Figs. S2 and S3 (ESI<sup>†</sup>). The composition of the NCs can be well correlated with the partial pressure of the

precursors (ESI†, Fig. S4). We obtained the lattice parameters of the end members (in a notation of  $Pnma$ ), which is consistent with the reference values;  $a=10.47$  Å,  $b=3.64$  Å,  $c=4.29$  Å for GeS;  $a=11.21$  Å,  $b=3.98$  Å,  $c=4.29$  Å for SnS;  $a=10.83$  Å,  $b=3.84$  Å,  $c=4.38$  Å for GeSe;  $a=11.52$  Å,  $b=4.16$  Å,  $c=4.42$  Å for SnSe.

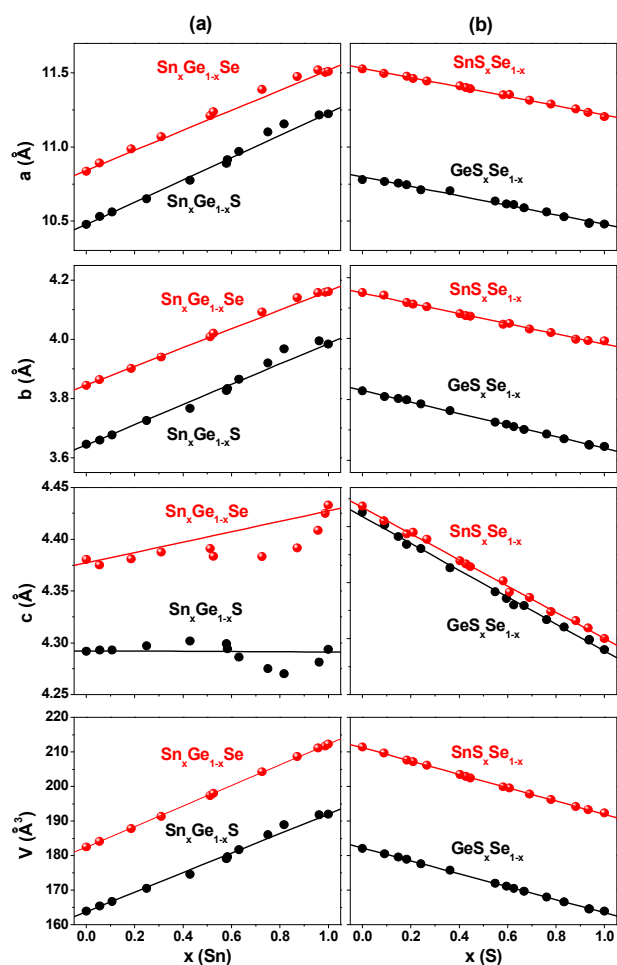


**Fig. 2** Dependence of the lattice constants ( $a$ ,  $b$ , and  $c$ ) and unit cell volume on Sn content ( $x$ ) in (a)  $\text{Sn}_x\text{Ge}_{1-x}\text{S}$  and  $\text{Sn}_x\text{Ge}_{1-x}\text{Se}$  NCs, and on S content ( $x$ ) in (b)  $\text{GeS}_x\text{Se}_{1-x}$  and  $\text{SnS}_x\text{Se}_{1-x}$  NCs.

Fig. 2 shows the lattice constants ( $a$ ,  $b$ , and  $c$ ) and the unit cell volume plotted as a function of  $x$ . In case of cation alloy ( $\text{Sn}_x\text{Ge}_{1-x}\text{S}$  and  $\text{Sn}_x\text{Ge}_{1-x}\text{Se}$ ) NCs, all three lattice constants varies nonlinearly with  $x$ . The deviation from a linear fit line (as drawn by a line) is called the “bowing” phenomenon. Analysis of this phenomenon in the present study using high-resolution synchrotron XRD clearly revealed the deviation. All data points an uncertainty of 5-10 %. The lattice constants  $a$  and  $b$  are larger than their linear values in the Sn-rich composition ( $x > 0.5$ ), which is referred to as “upward bowing”. The magnitude of the deviation is larger for the  $\text{Sn}_x\text{Ge}_{1-x}\text{S}$  NCs than for the  $\text{Sn}_x\text{Ge}_{1-x}\text{Se}$  NCs. In contrast, the  $c$  lattice constant shows a deviation in the opposite direction (referred to as “downward bowing”). It should be noted that the plots of the  $c$  lattice constant exaggerate its non-linear change owing to the smaller differences of binary counterparts (GeS-SnS and GeSe-SnSe). For  $\text{Sn}_x\text{Ge}_{1-x}\text{S}$  NCs, the

maximum deviations from the linear values occurs at  $x = 0.7$  with  $\Delta a = 0.08$  Å,  $\Delta b = 0.04$  Å, and  $\Delta c = -0.02$  Å. The maximum value of deviation in the lattice constants of  $\text{Sn}_x\text{Ge}_{1-x}\text{Se}$  NCs is  $\Delta a = 0.05$  Å,  $\Delta b = 0.02$  Å, and  $\Delta c = -0.03$  Å, at  $x = 0.8$ . The deviation of the  $c$  lattice constant was previously observed for the  $\text{Sn}_x\text{Ge}_{1-x}\text{Se}$  NCs and bulk materials.<sup>18,40</sup> The positive deviation (sum of  $\Delta a$  and  $\Delta b$ ) is constantly larger than the negative deviation ( $|\Delta c|$ ) for both NCs. As a result, the  $\text{Sn}_x\text{Ge}_{1-x}\text{S}$  NCs exhibit noticeably upward bowing in the unit cell volume, corresponding to the volume expansion. In the case of the  $\text{Sn}_x\text{Ge}_{1-x}\text{Se}$  NCs, the unit cell volume is changed almost linearly with  $x$ , owing to the less expansion of the  $a$  and  $b$  lattice constants compared to that of the  $\text{Sn}_x\text{Ge}_{1-x}\text{S}$  NCs.

Surprisingly, the  $\text{GeS}_x\text{Se}_{1-x}$  and  $\text{SnS}_x\text{Se}_{1-x}$  NCs showed no bowing in the lattice constants or the unit cell volume. This “no bowing” phenomenon of the  $\text{SnS}_x\text{Se}_{1-x}$  NCs is consistent with previous reports.<sup>16,41</sup> We concluded that the bowing of the lattice parameters exists in the cation alloy NCs. Both the  $\text{Sn}_x\text{Ge}_{1-x}\text{S}$  and  $\text{Sn}_x\text{Ge}_{1-x}\text{Se}$  NCs exhibit consistently anisotropic bowing: the upward bowing for the  $a$  and  $b$  constants and the downward bowing for the  $c$  constant in the range of  $x > 0.5$ . The dominant expansion of the lattice parameters upon the Sn-rich alloy formation was exclusively observed for these NCs. Furthermore, we used Raman spectroscopy to confirm the homogeneity of alloying (see ESI†, Fig. S5).

As mentioned in the introduction section, the double layer-type orthorhombic crystal structure can be described as a deformed rock salt structure. The interatomic distance perpendicular to these layers ( $a$ -axis) is larger than that along them ( $b$ - and  $c$ -axis). The deformation from the ideal rock-salt lattice is the greatest for the  $c$ -axis.<sup>42,43</sup> As a consequence, there exists considerable anisotropy of the physical properties. It was found that the location and nature of the band gap depends on the tightly bound crystallographic  $b$ - and  $c$ -axes; their indirect band gap is smaller for the  $c$ -axis than for the  $b$ -axis (*i.e.*, 1.542 *versus* 1.572 eV for GeS and 1.095 *versus* 1.142 eV for SnS).<sup>20,21</sup> Recent calculations showed a strong anisotropic band offset of SnS-GeS heterojunctions.<sup>44</sup>

The anisotropic bowing of the lattice constants is probably a result of the crystallographic anisotropy. The  $c$ -axis encloses the non-polar surface unlike the  $a$ - and  $b$ -axes. The bonding of the Sn-S lattice is more ionic than that of the Ge-S lattice.<sup>45</sup> Therefore, the incorporation of Sn into the Ge-S (or GeSe) lattices would be more favorable in polar  $a$ - and  $b$ -axes, such that the lattice constants  $a$  and  $b$  become larger than the linear value, whereas the  $c$  lattice constant reduces. As the Sn composition increases, the preference of the Sn-S bonds along the  $a$ - and  $b$ -axes would cause the expansion of the unit cell volume of  $\text{Sn}_x\text{Ge}_{1-x}\text{S}$ . For the  $\text{Sn}_x\text{Ge}_{1-x}\text{Se}$ , the expansion of the  $a$  and  $b$  lattice constants occurs by the less magnitude than that of the  $\text{Sn}_x\text{Ge}_{1-x}\text{S}$ , probably due to the more covalent character of GeSe-SnSe. No bowing phenomena of the anion alloys can be rationalized by the similar bonding nature of S and Se anions toward the same cations. For the bowing of the lattice constant of cubic phase crystals, Fong *et al.* suggested a model in which the bond-stretching or -bending force constants of the two constituents are critical to determine the curve shape.<sup>46</sup> In order to explain the anisotropic bowing curves of the orthorhombic phase crystals

using the force constants, a finer model is probably necessary.

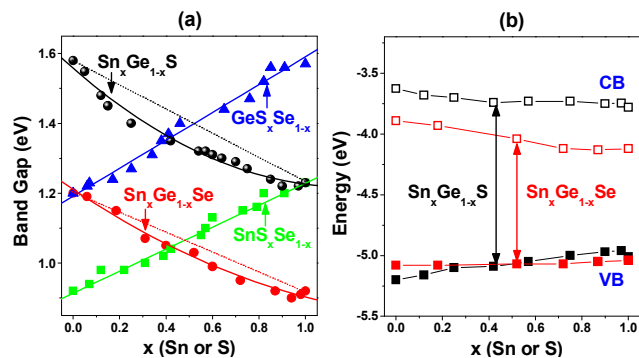


**Fig. 3** (a) Dependence of the optical band gap on the content ( $x$ ) of Sn or S, and (b) the band energy (VB and CB) diagram (*versus* vacuum level) of  $\text{Sn}_x\text{Ge}_{1-x}\text{S}$  and  $\text{Sn}_x\text{Ge}_{1-x}\text{Se}$ , which was estimated from the oxidation peaks of CV and optical band gap.

In addition, the optical band gap of all NC samples prepared in this study was estimated by using UV-visible-near IR (NIR) diffuse reflectance spectrum. The composition tuning enables the band gap to show absorption in the NIR region of 800–1400 nm (0.9–1.6 eV). Based on Kubelka–Munk (K–M) transformation, the plot of  $[F(v)h\nu]^{1/2}$  and  $[F(v)h\nu]^2$  (where  $F(v)$  is the diffuse reflectance spectrum) *versus* photon energy yielded the indirect and direct band gaps, respectively (see the ESI†, Fig. S6 and Table S2).<sup>27,38,39,47</sup> The indirect band gap ( $E_g$ ) is plotted in Fig. 3a. All these have uncertainty of at least 5 % that comes from the extrapolation process of the linear region. The  $E_g$  value of GeS (1.57 eV), SnS (1.23 eV), GeSe (1.20 eV), and SnSe (0.92 eV), is consistent with the reported value of the NC, respectively, 1.58 eV,<sup>27</sup> 1.18 eV,<sup>32</sup> 1.14 eV,<sup>27</sup> and 0.9 eV (size = 9 nm).<sup>36</sup> It is known that the bulk SnS exhibits a high absorption coefficient and excellent hole mobility with a direct band gap of 1.3 eV.<sup>48,49</sup> The plot of  $[F(v)h\nu]^2$  provides a direct band gap to be 1.25 eV, which is close to the value of the bulk. The steep rise of the absorption onset could be another evidence for the contribution of direct band gap. The small quantum confinement effects are probably due to the diameter being larger than the Bohr radius (e.g., 7 nm for SnS).<sup>32</sup>

The  $\text{Sn}_x\text{Ge}_{1-x}\text{S}$  NCs show a non-linear dependence of  $E_g$  on the composition, which deviates from the linear value, predicted using Vegard's law. This optical bowing is characterized by a positive bowing constant  $b$  (=0.25 eV), where  $E_g(x) = (1-x)E_g(\text{GeS}) + xE_g(\text{SnS}) - bx(1-x)$ . The  $\text{Sn}_x\text{Ge}_{1-x}\text{Se}$  NCs also show the optical bowing with  $b$  =0.14 eV, which is less than that of the  $\text{Sn}_x\text{Ge}_{1-x}\text{S}$  NCs. On the other hand, the anion alloys,  $\text{GeS}_x\text{Se}_{1-x}$  and  $\text{SnS}_x\text{Se}_{1-x}$ , NCs show no optical bowing;  $E_g$  changes almost linearly with the composition. Remarkably, the more significant bowing of the band gap appears in the  $\text{Sn}_x\text{Ge}_{1-x}\text{S}$  NCs that possess noticeably the expanded unit cell volume, which suggests that the optical bowing could be correlated with the bowing of the lattice parameters.

Zunger and coworkers explained the optical bowing of semiconductor alloys using the structure and electronic factors, which include the volume deformation of the band structure due to different lattice constants of the binary structures.<sup>50-53</sup> Recently, Wu *et al.* reported the calculation on the optical bowing ( $b > 0$ )

for the  $\text{Cd}_{1-x}\text{Zn}_x\text{S}$  cation alloy that is dominated by volume deformation.<sup>54</sup> There is no calculation to support the bowing phenomena of the Ge–Sn chalcogenide series. Thus, we are under theoretical investigation to rationalize the experimental results. Nevertheless, our results prove that the optical bowing of the cation alloy NCs is robustly related to the deformed volume; the expansion of the lattice parameters decreased the band gap, which is consistent with the general trend of II–VI semiconductor alloys.<sup>50,51,54</sup>

The cyclic voltammetric (CV) results were used to estimate their valence band position. The CV curves show the strong oxidation peaks with an onset in the range of 0.2–0.5 V, relative to the Ag/Ag<sup>+</sup> reference electrode (see the ESI†, Fig. S7 and Table S3). Based on the onset value of oxidation peak ( $E_{ox}$ ), the position of the valence band (VB) edge was estimated to be  $E_{VB} = -5.20$ ,  $-5.01$ ,  $-5.08$ , and  $-5.04$  eV from the vacuum level, for GeS, SnS, GeSe, and SnSe, respectively. Considering the  $E_g$  values (obtained from the UV-Vis-NIR spectrum), instead of using the weak reduction peak of the CV curves, the position of the CB was estimated to be  $E_{CB} = -3.63$ ,  $-3.78$ ,  $-3.89$ , and  $-4.12$  eV, for GeS, SnS, GeSe, and SnSe, respectively. It can be observed that the  $E_{VB}$  values of SnS are nearly equivalent to that of the bulk,  $-5.3$  eV.<sup>55</sup> The  $E_{VB}$  and  $E_{CB}$  values of SnSe NCs are close to that of the SnSe nanoflakes ( $E_{VB} = -4.85$  eV and  $E_{CB} = -3.80$  eV) reported recently in the literature.<sup>39</sup> The  $E_{VB}$  and  $E_{CB}$  values of the alloy samples are summarized in the ESI†, Table S3.

Fig. 3b shows the band-energy diagram of the  $\text{Sn}_x\text{Ge}_{1-x}\text{S}$  and  $\text{Sn}_x\text{Ge}_{1-x}\text{Se}$  NCs. Upon increasing the Sn composition ( $x$ ), the  $E_{VB}$  value of the  $\text{Sn}_x\text{Ge}_{1-x}\text{S}$  and  $\text{Sn}_x\text{Ge}_{1-x}\text{Se}$  NCs shifts to a more positive energy by 0.19 and 0.04 eV, respectively. The  $E_{VB}$  value of GeSe is more positive than that of GeS by 0.12 eV. On the other hand, the  $E_{VB}$  value of SnSe is slightly more negative than that of SnS by 0.03 eV, which is the same as that of PbS–PbSe.<sup>52</sup> This means that the VB offset of GeSSe, SnSSe, and PbSSe is 0.12,  $-0.03$ , and  $-0.03$  eV, respectively. The results are consistent with the general trend that the VB maximum energies *increase* with increasing cation and anion atomic number, and the VB offset *decreases* with increasing cation atomic number (e.g., 0.50 eV for ZnSSe and 0.42 eV for CdSSe).<sup>51,56</sup> The CB of  $\text{Sn}_x\text{Ge}_{1-x}\text{S}$  and  $\text{Sn}_x\text{Ge}_{1-x}\text{Se}$  shifts to a more negative energy with increasing  $x$  by about 0.2 eV. All the NCs prepared in this study have a CB lying at 3.6–4.1 eV below the vacuum level. In order to explore their potential application in photovoltaic cells, we further monitored the generation of the photoelectrons, as follows.

The NCs were deposited onto an ITO substrate, and a PEC cell was constructed with a Pt counter electrode and 0.1 M  $\text{Na}_2\text{SO}_4$  electrolyte, so as to monitor the photocurrent response. Fig. 4a shows the transient photocurrent responses of the NC film at  $E = -0.5$  V *versus* Ag/AgCl reference electrode under 100 mW/cm<sup>2</sup> AM 1.5G illumination. The electrodes were prompt in generating negative photocurrent ( $\Delta I$ ) with a reproducible response to on/off cycles (10 s), demonstrating the typical *p*-type photoconductivity.<sup>34</sup> The average photocurrent  $\Delta I$  for GeS,  $\text{Sn}_{0.4}\text{Ge}_{0.6}\text{S}$ ,  $\text{Sn}_{0.9}\text{Ge}_{0.1}\text{S}$ , and SnS, was observed to be 0.2, 2, 2, and 0.8  $\mu\text{A}/\text{cm}^2$ , respectively, showing an enhancement effect of alloy NCs. On the other hand, the GeSeSe series also exhibit *p*-type behavior, but with negligible enhancement effects.

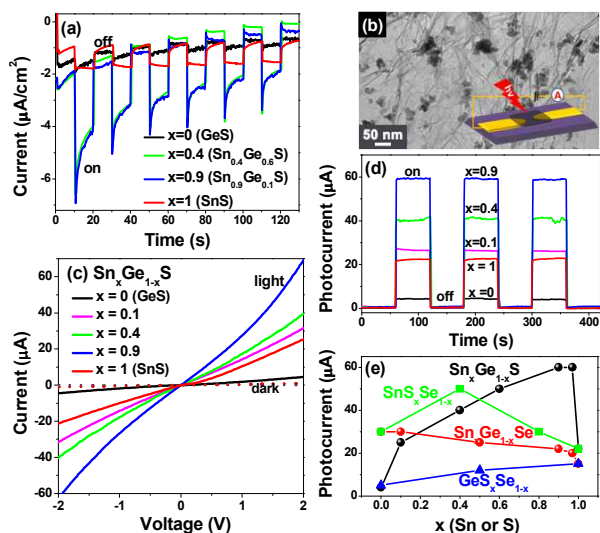


**Fig. 4** (a) Transient photocurrent of the  $\text{Sn}_x\text{Ge}_{1-x}\text{S}$  ( $x = 0, 0.4, 0.9,$  and  $1$ ) NC film on an ITO substrate in a PEC cell at an applied voltage of  $-0.5$  V under  $100 \text{ mW/cm}^2$  AM 1.5G illumination, turned on and off at intervals of  $10$  s. (b) TEM image of the NC-RGO hybrid and a schematic diagram representing the photodetector device. (c)  $I$ - $V$  characteristics of  $\text{Sn}_x\text{Ge}_{1-x}\text{S}$  ( $x = 0, 0.1, 0.4, 0.9,$  and  $1$ ) NC-RGO under  $514 \text{ nm}$  ( $10 \text{ mW}$ ) irradiation and in darkness. (d)  $\Delta I$ - $t$  curves at a bias voltage of  $2$  V under chopped irradiation. (e) Photocurrents of  $\text{Sn}_x\text{Ge}_{1-x}\text{S}$ ,  $\text{Sn}_x\text{Ge}_{1-x}\text{Se}$ ,  $\text{Sn}_x\text{Ge}_{1-x}\text{S}_2$ ,  $\text{GeS}_x\text{Se}_{1-x}$ , and  $\text{SnS}_x\text{Se}_{1-x}$ -RGO as a function of Sn or S content ( $x$ ).

To gain further insight on their pertinent properties for optoelectronic devices, we also measured the photocurrents of the NCs deposited onto reduced graphene oxide (RGO). Fig. 4b shows the TEM image of the typical 1:1 wt. ratio NC-RGO hybrid nanostructures, which indicates that the NCs are homogeneously anchored onto the RGO nanosheets. The inset shows the schematic diagram of the photodetector fabricated by using the DEP technique. The nanosheet of NC:RGO was deposited between the Ti/Au electrodes separated by a gap of  $2 \mu\text{m}$  onto a silicon oxide substrate.

Fig. 4c shows the current-voltage ( $I$ - $V$ ) curves of the photodetector composed of  $\text{Sn}_x\text{Ge}_{1-x}\text{S}$ -RGO hybrid, under dark conditions and irradiation at  $514 \text{ nm}$  ( $2.4 \text{ eV}$ ) using an Ar ion laser ( $10 \text{ mW}$ ). The  $I$ - $V$  curves were linear and symmetric within the measured range ( $-2$  to  $2$  V), indicating good ohmic contact in the device. Upon irradiation, the photocurrents increased linearly with light intensity ( $2$ – $10 \text{ mW}$ ). The transient photocurrents ( $\Delta I$ ) at a bias voltage of  $2$  V were collected with light on/off cycles (Fig. 4d). The photocurrent depended on the composition, distinctively with the higher value of the alloys, as compared with that of their binary counterparts. The much higher photocurrent was observed in the Sn-rich composition. The photosensitivity, defined as the ratio of  $\Delta I$  to the current under dark conditions, reached a maximum value of  $20$ . In addition, we also measured the photocurrent from the  $\text{Sn}_x\text{Ge}_{1-x}\text{Se}$ -RGO photodetectors. As the Sn content ( $x$ ) increases, the photocurrent decreases rather monotonically with a slight enhancement in the Sn-rich composition. On the other hands, the photocurrent from the anion alloy NC-RGO photodetectors showed the enhancement of alloys for the only  $\text{SnS}_x\text{Se}_{1-x}$ -RGO. Fig. 4e shows the photocurrent of the cation and anion alloy NC-RGO photodetectors as a function of  $x$ .

Once the excitons are created by the light absorption of the NC, the photoelectrons are directly transferred from their CB ( $3.6$ – $4.1 \text{ eV}$  below the vacuum level) to RGO (work function is  $4.5 \text{ eV}$ ), resulting in a flow toward positive charged electrode. The photogenerated electron-hole pairs separate through the binding between the NC and RGO, creating a large photocurrent. In order to explain the enhancement of photoconversion efficiency of  $\text{Sn}_x\text{Ge}_{1-x}\text{S}$  and  $\text{SnS}_x\text{Se}_{1-x}$  alloy NCs, we suggest that the SnS composition induces the direct band gap character of the alloy NCs, which may allow more efficient photon absorption and the subsequent generation and separation of electron-hole pairs, thereby increasing photocurrent. We believe that the SnGeS- and SnSSe-RGO hybrid nanostructures prepared in this study hold great promise for use in transparent flexible photodetectors that respond sensitively over the UV-visible-NIR wavelength region.

## Conclusion

We report the successful synthesis of composition-tuned  $\text{Sn}_x\text{Ge}_{1-x}\text{S}$ ,  $\text{Sn}_x\text{Ge}_{1-x}\text{Se}$ ,  $\text{GeS}_x\text{Se}_{1-x}$ , and  $\text{SnS}_x\text{Se}_{1-x}$  alloy NCs over the entire compositional range ( $0 \leq x \leq 1$ ) by a facile gas-phase laser photolysis method. The ternary compositions of the NCs were precisely tuned by precise control of the partial pressure of the precursors, namely, TMG, TMT,  $\text{H}_2\text{S}$ , and DMS. Four series of the orthorhombic phase alloy NCs prepared in this study covered a wide range of band gaps ( $0.9$ – $1.6 \text{ eV}$ ). XRD peak analysis revealed unique anisotropic bowing phenomena of the lattice constants for the cation alloys ( $\text{Sn}_x\text{Ge}_{1-x}\text{S}$  and  $\text{Sn}_x\text{Ge}_{1-x}\text{Se}$ ) NCs. Remarkably, the  $\text{Sn}_x\text{Ge}_{1-x}\text{S}$  and  $\text{Sn}_x\text{Ge}_{1-x}\text{Se}$  NCs exhibited an optical bowing with a bowing constant of  $0.25$  and  $0.14 \text{ eV}$ , respectively, which is correlated with the increase of the lattice parameters. On the other hand, the anion alloy ( $\text{GeS}_x\text{Se}_{1-x}$ , and  $\text{SnS}_x\text{Se}_{1-x}$ ) NCs showed no optical bowing or lattice parameter bowing.

Using the UV-visible-NIR spectrum and CV data, we estimated the band-gap position, whose VB and CB locate at  $5.0$ – $5.2 \text{ eV}$  and  $3.6$ – $4.1 \text{ eV}$  below the vacuum level, respectively, below the vacuum level. The photodetectors composed of a  $\text{Sn}_x\text{Ge}_{1-x}\text{S}$ - and  $\text{SnS}_x\text{Se}_{1-x}$ -RGO hybrid showed the significant enhancement of the alloy composition. Based on these results, we suggest that the SnS composition induces the direct band gap character of the alloy NCs. This result provides a benchmark for the alloy effect that has recently attracted much attention in the field of photoconversion devices.

## Acknowledgments

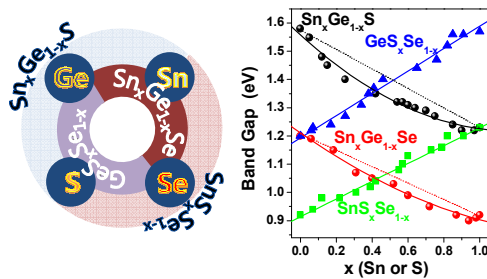
This study was supported by NRF (2011-0015235; 2011-0020090; 2011-0013070), WCU (R31-2012-000-10035-0), and KETEP (20104010100640). The HVEM and XPS (Pusan) measurements were performed at the KBSI. The experiments at the PLS were partially supported by MOST and POSTECH.

## Notes and references

Department of Chemistry, Korea University, Jochiwon 339-700, Korea.  
\* Corresponding Author: [parkjh@korea.ac.kr](mailto:parkjh@korea.ac.kr)

† Electronic Supplementary Information (ESI) available: [Table S1-S3, Fig. S1-S7. XRD pattern, EDX data, Raman spectrum, Kubelka-Munk transformation data of UV-visible-NIR absorption spectrum, and CV curves]. See DOI: 10.1039/b000000x/

- 1 Y D. V. Talapin, J. S. Lee, M. V. Kovalenko and E. V. Shevchenko, *Chem. Rev.*, 2010, **110**, 389.
- 2 A. J. Nozik, M. C. Beard, J. M. Luther, M. Law, R. J. Ellingson and J. C. Johnson, *Chem. Rev.*, 2010, **110**, 6873.
- 3 G. Konstantatos and E. H. Sargent, *Nat. Nanotech.*, 2010, **5**, 391.
- 4 L. A. Padilha, J. T. Stewart, R. L. Sandberg, W. K. Bae, W. -K. Koh, J. M. Pietryga and V. I. Klimov, *Acc. Chem. Res.*, 2013, **46**, 1261.
- 5 W. Ma, J. M. Luther, H. Zheng, Y. Wu and A. P. Alivisatos, *Nano Lett.*, 2009, **9**, 1699.
- 6 D. K. Smith, J. M. Luther, O. E. Semonin, A. J. Nozik and M. C. Beard, *ACS Nano*, 2011, **5**, 183.
- 7 J. Akhtar, M. Afzaal, M. Banski, A. Podhorodecki, M. Syperek, J. Misiewicz, U. Bangert, S. J. O. Hardman, D. M. Graham, W. R. Flavell, D. J. Binks, S. Gardonio and P. O'Brien, *J. Am. Chem. Soc.*, 2011, **133**, 5602.
- 8 A. C. Onicha, N. Petchsang, T. H. Kosel and M. Kuno, *ACS Nano*, 2012, **6**, 2833.
- 9 J. W. Thomson, X. Wang, L. Hoch, D. Faulkner, S. Petrov and G. A. Ozin, *J. Mater. Chem.*, 2012, **22**, 5984.
- 10 A. G. Midgett, J. M. Luther, J. T. Stewart, D. K. Smith, L. A. Padilha, V. I. Klimov, A. J. Nozik and M. C. Beard, *Nano Lett.*, 2013, **13**, 3078.
- 11 Z. Liu, Y. Sun, J. Yuan, H. Wei, X. Huang, L. Han, W. Wang, H. Wang and W. Ma, *Adv. Mater.*, 2013, **25**, 5772.
- 12 I. U. Arachchige and M. G. Kanatzidis, *Nano Lett.*, 2009, **9**, 1583.
- 13 H. Wei, Y. Su, S. Chen, Y. Lin, Z. Yang, H. Sun and Y. Zhang, *CrystEngComm.*, 2011, **13**, 6628.
- 14 R. B. Soriano, C. D. Malliakas, J. Wu and M. G. Kanatzidis, *J. Am. Chem. Soc.*, 2012, **134**, 3228.
- 15 J. He, S. N. Girard, J. C. Zheng, L. Zhao, M. G. Kanatzidis and V. P. Dravid, *Adv. Mater.*, 2012, **24**, 4440.
- 16 H. Wei, Y. Su, S. Chen, Y. Lin, Z. Yang, X. Chen and Y. Zhang, *J. Mater. Chem.*, 2011, **21**, 12605.
- 17 H. S. Im, Y. Myung, Y. J. Cho, C. H. Kim, H. S. Kim, S. H. Back, C. S. Jung, D. M. Jang, Y. R. Lim, J. Park and J. P. Ahn, *RSC Adv.*, 2013, **3**, 10349.
- 18 J. J. Buckley, F. A. Rabuffetti, H. L. Hinton and R. L. Brutchey, *Chem. Mater.* **2012**, **24**, 3514.
- 19 Y. Myung, H. S. Im, C. H. Kim, C. S. Jung, Y. J. Cho, D. M. Jang, H. S. Kim, S. H. Back and J. Park, *J. Chem. Commun.*, 2013, **49**, 187.
- 20 A. M. Elkorashy, *J. Phys. C: Solid State Phys.*, 1988, **21**, 2595.
- 21 A. P. Lambros, D. Geraleas and N. A. Economou, *J. Phys. Chem. Solids*, 1974, **35**, 537.
- 22 A. M. Elkorashy, *Phys. Status Solidi B*, 1986, **135**, 707.
- 23 L. Makinistian, E. A. Albanesi, *J. Phys.: Condens. Matter*, 2007, **19**, 186211.
- 24 A. M. Elkorashy, *J. Phys. Chem. Solids*, 1986, **47**, 497.
- 25 B. Pejova and A. Tanuševski, *J. Phys. Chem. C*, 2008, **112**, 3525.
- 26 S. M. Yoon, H. J. Song, H. C. Choi, H. C. Adv. Mater., 2010, **22**, 2164.
- 27 D. D. Vaughn II, R. J. Patel, M. A. Hickner and R. E. Schaak, *J. Am. Chem. Soc.*, 2010, **132**, 15170.
- 28 D. J. Xue, J. Tan, J. S. Hu, W. Hu, Y. G. Guo and L. J. Wan, *Adv. Mater.*, 2012, **24**, 4528.
- 29 S. G. Hickey, C. Waurisch, B. Rellinghaus, and A. Eychmüller, *J. Am. Chem. Soc.* 2008, **130**, 14978.
- 30 Y. Wang, H. Gong, B. Fan and G. Hu, *J. Phys. Chem. C*, 2010, **114**, 3256.
- 31 J. Chao, Z. Xie, X. B. Duan, Y. Dong, Z. Wang, J. Xu, B. Liang, B. Shan, J. Ye, D. Chen and G. Shen, *CrystEngComm*, 2012, **14**, 3163.
- 32 Z. Deng, D. Cao, J. He, S. Lin, S. M. Lindsay and Y. Liu, *ACS Nano*, 2012, **6**, 6197.
- 33 J. Chao, Z. Wang, X. Xu, Q. Xiang, W. Song, G. Chen, J. Hu and D. Chen, *RSC Adv.*, 2013, **3**, 2746.
- 34 M. Steichen, R. Djemour, L. Gütay, J. Guillot, S. Siebentritt and P. J. Dale, *J. Phys. Chem. C*, 2013, **117**, 4383.
- 35 M. A. Franzman, C. W. Schlenker, M. E. Thompson and R. L. Brutchey, *J. Am. Chem. Soc.*, 2010, **132**, 4060.
- 36 W. J. Baumgardner, J. J. Choi, Y. F. Lim and T. Hanrath, *J. Am. Chem. Soc.*, 2010, **132**, 9519.
- 37 S. Liu, X. Guo, M. Li, W. H. Zhang, X. Liu and C. Li, *Angew. Chem. Int. Ed.*, 2011, **50**, 12050.
- 38 K. Jang, I. Y. Lee, J. Xu, J. Choi, J. Jin, J. H. Park, H. J. Kim, G. H. Kim and S. U. Son, *Cryst. Growth Des.*, 2012, **12**, 3388-3391.
- 39 L. Li, Z. Chen, Y. Hu, X. Wang, T. Zhang, W. Chen and Q. Wang, *J. Am. Chem. Soc.*, 2013, **135**, 1213.
- 40 V. H. Krebs and D. Langer, *Z. Anorg. Allg. Chem.*, 1964, **334**, 37.
- 41 P. Boudjouk, D. J. Seidler, D. Grier and G. McCarthy, *Chem. Mater.*, 1996, **8**, 1189.
- 42 W. H. Zachariasen, *Phys. Rev.*, 1932, **40**, 917.
- 43 H. Wiedemeier and H. G. von Schnering, *Z. Kristallogr.*, 1978, **148**, 295.
- 44 B. D. Malone and E. Kaxiras, *Phys. Rev. B*, 2013, **87**, 245312.
- 45 R. B. Shalvoy, G. B. Fisher and P. J. Stiles, *Phys. Rev. B*, 1977, **15**, 1680.
- 46 C. Y. Fong, W. Weber and J. C. Phillips, *Phys. Rev. B*, 1976, **14**, 5387.
- 47 A. Hagfeldt and M. Grätzel, *M. Chem. Rev.*, 1995, **95**, 49.
- 48 M. Parenteau and C. Carolne, *Phys. Rev. B*, 1990, **41**, 5227.
- 49 K. Ramasamy, V. L. Kuznetsov, K. Gopal, M. A. Malik, J. Raftery, P. P. Edwards and P. O'Brien, *Chem. Mater.*, 2013, **25**, 266.
- 50 J. E. Bernard and A. Zunger, *Phys. Rev. B*, 1987, **36**, 3199.
- 51 S. H. Wei, and A. Zunger, *Phys. Rev. B*, 1988, **37**, 8958.
- 52 S. H. Wei and A. Zunger, *Phys. Rev. B*, 1997, **55**, 13605.
- 53 S. H. Wei, S. B. Zhang and A. Zunger, *J. Appl. Phys.*, 2000, **87**, 1304.
- 54 J. C. Wu, J. Zheng, C. L. Zacherl, P. Wu, Z. K. Liu and R. Xu, *J. Phys. Chem. C*, 2011, **115**, 19741.
- 55 M. Sugiyama, K. T. R. Reddy, N. Revathi, Y. Shimamoto and Y. Murata, *Thin Solid Films*, 2011, **519**, 7429.
- 56 Y. H. Li, A. Walsh, S. Chen, W. J. Yin, J. H. Yang, J. Li, J. L. F. Da Silva and S. H. Wei, *Appl. Phys. Lett.*, 2009, **94**, 212109.



$\text{Sn}_x\text{Ge}_{1-x}\text{S}$ ,  $\text{Sn}_x\text{Ge}_{1-x}\text{Se}$ ,  $\text{GeS}_x\text{Se}_{1-x}$ , and  $\text{SnS}_x\text{Se}_{1-x}$  alloy nanocrystals were synthesized by novel gas-phase laser photolysis. Their composition-dependent lattice parameters and band gap were thoroughly characterized. The  $\text{Sn}_x\text{Ge}_{1-x}\text{S}$  and  $\text{SnS}_x\text{Se}_{1-x}$  nanocrystals exhibit higher photoconversion efficiency as compared with the end members.